

Electronic properties of magnetic semiconductor CuMnO_2 : a first principles study

Apurba Sarkar,¹ Joydeep Chatterjee,² Soumya Mukherjee,³ Arghya Taraphder,² and Nandan Pakhira¹

¹Department of Physics, Kazi Nazrul University, Asansol-713340, West Bengal, India

²Department of Physics, Indian Institute of Technology Kharagpur, Kharagpur-721302, West Bengal India

³Department of Metallurgical Engineering, School of Mines and Metallurgy, Kazi Nazrul University, Asansol-713340, West Bengal, India

Geometrically frustrated magnetic semiconductor CuMnO_2 has potential applications as photo-catalyst, in photochemical cells and multi-ferroic devices. Electronic band structure in the antiferromagnetic and ferromagnetic phases of CuMnO_2 were calculated using first principle density functional theory (DFT) as implemented in VASP. Electronic band structure in the antiferromagnetic state shows indirect band gap (~ 0.53 eV) where as in the ferromagnetic state it shows half-metallic state with 100% spin polarization. The half-metallic state arises due to *double exchange* mechanism. In the half-metallic state the density of states for the up spin channel shows asymmetric power law behaviour near the Fermi level while the down spin channel shows fully gapped behaviour. The calculated magnetic moment of Mn atom in the ferromagnetic ($3.70 \mu_B$) and antiferromagnetic ($3.57 \mu_B$) states are consistent with experimental values. Our calculation predicts potential application of CuMnO_2 in spintronic devices especially in the ferromagnetic state, as a spin injector for spin valves in spintronic devices.

I. INTRODUCTION

Magnetic semiconductors such as full Heusler alloys¹, half Heusler alloys^{2,3}, diluted magnetic semiconductors (DMS)⁴ etc. have been commercially used for the fabrication of spintronic devices. Geometrically frustrated magnetic semiconductors with chemical formula ABO_2 ($A = \text{Cu, Ag}$; $B = \text{Fe, Cr, Mn, Co, Ni}$) have attracted a lot of attention due to their diverse and fascinating electronic and magnetic properties as well as their potential technological applications such as multi-ferroic oxide materials, photovoltaic and photo-catalytic semiconductors, thermo- electric materials etc.⁵⁻⁸. Some of the materials (like, CuFeO_2 , CuCrO_2 , NaCoO_2)⁹⁻¹¹ showing triangular-lattice antiferromagnetic (TLA) state have layered delafossite structure as shown in Fig. 1, where the monovalent A^+ cations are linearly coordinated with two O^{-2} ions, forming O-A-O dumbbells and trivalent B^{3+} cations are surrounded by six O^{-2} ions, forming BO_6 edge-sharing-octahedral layers. These two layers are stacked along the c -axis. The two-layer repeating structure belongs to the space group P63/mmc with 2H hexagonal symmetry while the three layer repeating structure belongs to the space group $\text{R}\bar{3}\text{m}$ with 3R rhombohedral symmetry. These class of semiconducting magnetic materials show giant magneto-resistance (GMR), tunnel magneto-resistance (TMR) as well as anisotropic magneto-resistance (AMR)^{4,12}.

Another example of geometrically frustrated magnetic system is CuMnO_2 (crednerite). CuMnO_2 is chemically stable (over pH range 7-14), transparent p -type semiconductor with direct band gap in the visible region and hence absorbs a large part of sunlight. This material has potential application as photo-catalyst, in photochemical cells, multiferroic devices, etc.¹³⁻¹⁵. In previous studies^{16,17} it has been shown that CuMnO_2 exhibits two types of magnetic ordering. At low temperatures, ($T < T_N = 65\text{K}$) it shows three-dimensional antiferro-

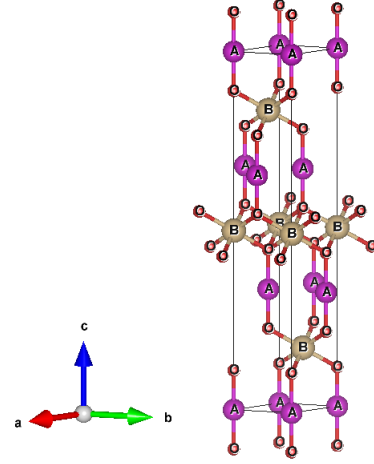


FIG. 1: Conventional unit cell of rhombohedral (space group $\text{R}\bar{3}\text{m}$) delafossite compound ABO_2 ($A = \text{Cu, Ag}$; $B = \text{Fe, Cr, Mn, Co, Ni}$). The structure consists of layers of slightly distorted octahedral BO_6 separated by the O-A-O linear linkage.

magnetic (AFM) spin ordering where as ferromagnetic (FM) spin ordering at high temperatures and behaves like metal¹⁷. On the other hand, AFM CuMnO_2 is insulating with band gap of 0.2 eV¹⁸. It is interesting to mention that ferromagnetic semiconductors with strong spin polarization can be used as spin injector for spin valves in spintronic devices. Antiferromagnetic semiconductors like bulk SrIr_2O_4 ¹⁹, Cr-Doped Ge-Core/Si-Shell nanowires²⁰, porous boron nitride (B_6N_6) sheet²¹, 2D monolayers of MnSi_2N_4 ²² have many potential applications in future spintronic devices. In this context, geometrically frustrated CuMnO_2 , because of its unique magnetic properties, is one of the most promising mate-

rial for spintronic devices.

To the best of our knowledge there is no reported theoretical study on the electronic structure of spin-polarized CuMnO_2 . In this work, using first principle density functional theory (DFT)²³, we have investigated the electronic structures and density of states for both the anti-ferromagnetic (AFM) and ferromagnetic (FM) states of CuMnO_2 . We find that the anti-ferromagnetic state is a small bandgap semiconductor while the ferromagnetic state is a half-metal with 100% spin polarization. It is interesting to mention that, Ismail et. al.²⁴, using first principles DFT, have reported half-metallic behavior of a new class of delafossite material with chemical formula SMoO_2 ($S = \text{Na, K, Rb, Cs}$). The organization of the rest of the paper is as follows : in Sec. II we discuss about the crystal structure of CuMnO_2 , in Sec. III we provide the computational details. Then in Sec. IV we discuss our results for both type of magnetically ordered states, in Sec. V we discuss about the magnetic properties of the system in both the phases and finally in Sec. VI we conclude.

II. CRYSTAL STRUCTURE

CuMnO_2 has monoclinic structure belonging to the space group $C2/m$. The monoclinic $C2/m$ structure instead of the usual rhombohedral $R\bar{3}m$ structure arises due to lattice distortion in the presence of Jahn-Teller effect on the Mn^{3+} ions in the crystal-field split e_g orbital manifold of d^4 electronic configuration ($t_{2g}^3 e_g^1$). The optimized crystal structure of CuMnO_2 is shown in Figure 1 (a) and (b). In this structure alternating MnO_6 octahedral layers are separated by O-Cu-O layer along the c -axis. There are two short and four long distances for each Mn atom which significantly effects the magnetic arrangement of Mn^{3+} cations and frustrates the system. In each unit cell there are 2 Cu, 2 Mn and 4 O atoms. In Table I we show the the Wyckoff positions of various atoms. The system is topologically representative of a frustrated square lattice with nearest neighbour (J_1) and next nearest neighbour (J_2) interactions. This frustration gets relieved through a magneto-elastic coupling to the lattice as evidenced by a structural phase transition, associated with magnetic ordering, from a monoclinic ($C2/m$) to a strained triclinic $C\bar{1}$ phase.

TABLE I: Atomic positions of various elements

Wyckoff	element	x	y	z
2a	Mn	0	0	0
2d	Cu	0	0.5	0.5
4i	O	0.904961	0.5	0.179972

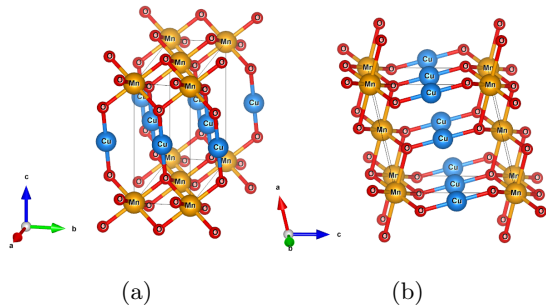


FIG. 2: (a) and (b) are the standard and side view of the optimized crystal structure of CuMnO_2 (Space group $C2/m$).

III. COMPUTATIONAL DETAILS

All the calculations were performed using the density functional theory (DFT) framework, as implemented in the VASP code²⁵. To treat the exchange and correlations effect between core and valence electrons, we used the Perdew-Burke-Ernzerhof (PBE)²⁶ exchange-correlation (XC) functionals in the frame work of generalized gradient approximation (GGA)²⁷ and projector augmented wave (PAW)²⁸ basis. The experimental lattice parameters and atomic positions of CuMnO_2 were taken from material project website. The constituent atoms and their valance state are: Cu : $[\text{Ar}]3d^{10}4s^1$, Mn : $[\text{Ar}]3d^4$ and O : $1s^2 2s^2 2p^6$, respectively. The atomic positions, lattice vectors, cell angles and the cell volume were allowed to relax. The optimized lattice parameters along with their experimental values are summarized in Table II. The convergence criterion for energy and force were set to 10^{-8} eV and 0.001 eV/Å, respectively. We have used an energy-cutoff 520 eV and a $15 \times 15 \times 15$ Monkhorst-Pack²⁹ k -mesh for structural optimization and GGA selfconsistent calculation while for the density of states (DOS) calculation, we have used a denser Monkhorst-Pack $25 \times 25 \times 25$ k -mesh. The Brillouin-zone (BZ) integration was performed on Γ centered symmetry reduced Monkhorst-Pack meshes using a Gaussian smearing with $\sigma = 0.05$ eV. The electronic band structure was plotted along the paths involving high symmetry points $\Gamma, C, C_2, Y_2, M_2, D, D_2, A, V_2$. Calculated bands were plotted along the high symmetry directions $\Gamma - C, C_2 - Y_2 - \Gamma - M_2 - D, D_2 - A - \Gamma - V_2$. Crystal structure visualization and analysis were performed using the VESTA³⁰ software. GGA+U calculations were also carried out with on-site Coulomb repulsion term. We used $U_{\text{eff}} = U - J_H = 4.1$ eV for Mn atoms which is consistent with the previously reported values¹⁷.

TABLE II: Comparison between experimental and calculated (this work) lattice constants of CuMnO_2 under GGA approximation.

System	Experimental			GGA		
	$a(\text{\AA})$	$b(\text{\AA})$	$c(\text{\AA})$	$a(\text{\AA})$	$b(\text{\AA})$	$c(\text{\AA})$
CuMnO_2	5.58	2.88	5.89	5.68	2.89	5.90

IV. RESULTS AND DISCUSSIONS

In Table II we compare the lattice constants obtained from structural relaxation under GGA against their observed experimental values. As can be clearly observed, the calculated values are very close to the observed experimental values. This validates the computed relaxed structures against their observed lattice structure. From the relaxed structure we calculated the self-consistent field and subsequently the electronic band structure and density of states. We consider both type of magnetically ordered states.

A. Electronic structure of Antiferromagnetic CuMnO_2

We first consider the antiferromagnetically ordered state. According to Damay et. al.¹⁶ the low temperature magnetic order with propagation vector $\mathbf{k} = (-\frac{1}{2}, \frac{1}{2}, \frac{1}{2})$ is described as spins antiferromagnetically aligned along $[1 -1 0]$ and ferromagnetically aligned along $[1 1 0]$, corresponding to collinear antiferromagnetic order predicted for a frustrated two-dimensional antiferromagnetic Heisenberg model on a square lattice for $J_2/J_1 > 0.5$ in the presence of spin-lattice coupling.

In Fig. 3 we show the electronic band structure of CuMnO_2 in the antiferromagnetic state, calculated under GGA and GGA+U approximations. As stated earlier, the bands are plotted along various high symmetry directions and the Fermi level is set to zero. The calculated band structure shows that CuMnO_2 in the antiferromagnetic state is an indirect semiconductor with band gap 0.53 eV. The valence band maximum (VBM) is situated at the Γ point while the conduction band minimum (CBM) is located at the D point and is indicated by the dotted arrow. Under GGA+U approximation the indirect band gap increases by 0.02 eV. In order to understand the characteristics and detailed orbital structure, we also have calculated the total as well as partial density of states for various atoms. In Fig. 4 and Fig. 5 we have shown the total density of states (TDOS) as well as the partial density of states (PDOS) of each atom in the low temperature antiferromagnetic phase under GGA and GGA+U approximations, respectively. Further, we also have shown orbital resolved partial density of states for each atom in a given unit cell. The total as well as partial density of states show a clear gap at the Fermi level, consistent with the semiconducting nature of the antifer-

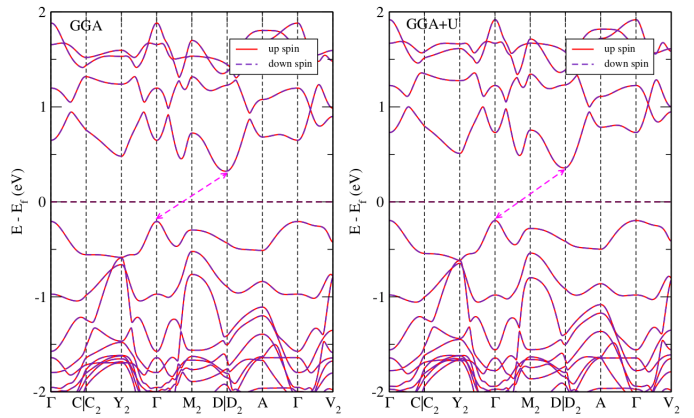


FIG. 3: Electronic band structure in the antiferromagnetic state of CuMnO_2 , calculated under GGA [panel (a)] and GGA+U [panel (b)] approximations. The Fermi energy is set to 0 eV.

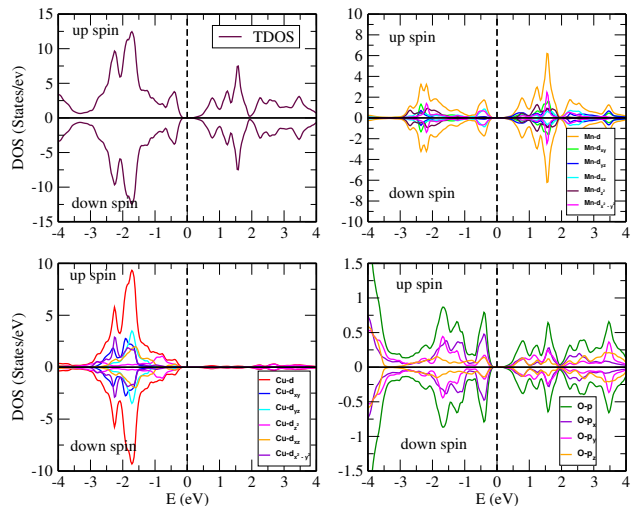


FIG. 4: Total and partial density of states of CuMnO_2 in the anti-ferromagnetic state under GGA approximations. The Fermi level is set to 0 eV.

romagnetic state. The density of states away from the Fermi level is dominated by broad peaks arising due to Mn-3d and Cu-3d orbitals. In particular the broad peak at -0.4 eV corresponding to the VB arises mainly due to hybridization between Mn $3d_{x^2-y^2}$, $3d_{xz}$ and O $2p_x$, $2p_y$ and $2p_z$ orbitals. This is expected as in MnO_6 octahedra each Mn^{3+} cation is in $d^4(t_{2g}^3 e_g^1)$ state. The VB as well as antiferromagnetic ordering arises due to overlap between Mn $3d_{x^2-y^2}$ and O $2p_x$, $2p_y$ orbital along each Mn-O-Mn bond giving rise to antiferromagnetic $e_g - e_g$ superexchange between half-filled e_g orbitals. Also two Mn $3d_{xz}$ orbitals of two neighbouring MnO_6 octahedra can overlap via O $2p_z$ orbitals giving rise to antiferromagnetic $t_{2g} - t_{2g}$ superexchange. The broad spectral features in the range -4 eV to -1 eV arises mainly due to Cu 3d orbitals

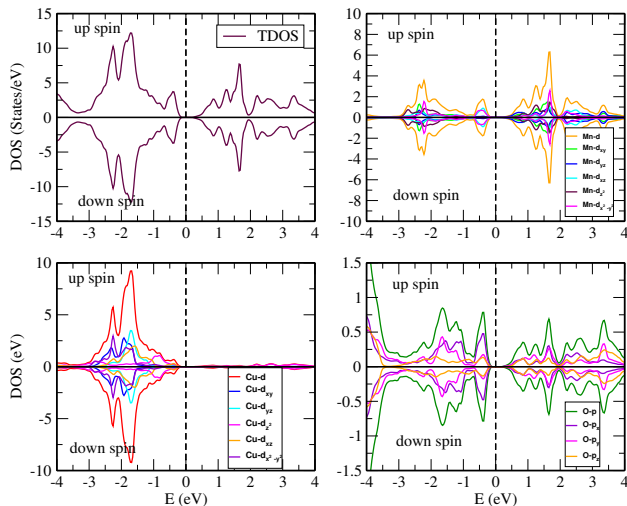


FIG. 5: Total and partial density of states of CuMnO_2 in the anti-ferromagnetic state under GGA+U approximations. The Fermi level is set to 0 eV.

present in each O-Cu-O layer along the c -axis. The conduction band arises due to transition between various hybridized Mn-3d and O-2p orbitals. The conduction band peaks between +1 eV to +2 eV are much sharper than the peaks of the valence band. The origin of these peaks are due to transitions between crystal field split Mn-3d orbitals which maintains very strong atomic character. The conduction band minimum is mainly composed of Mn-3d states with the minor contribution of O-p states indicating some Mn-O interactions. The symmetric nature of the TDOS for both the up and down spin channel confirms the antiferromagnetic nature of the ground state.

B. Electronic structure of Ferromagnetic CuMnO_2

Next we consider the ferromagnetic state of CuMnO_2 . It has been reported^{16,17,31,32} that the high temperature state of CuMnO_2 is ferromagnetic in nature. In Fig. 6 we have shown spin-polarized electronic band structure in the ferromagnetic state of CuMnO_2 under GGA [panel (a)] and GGA+U [panel (b)] approximations. As can be clearly observed electronic bands corresponding to the down spin channel shows semiconducting nature while for the up spin channel some bands touch the Fermi level and hence shows the metallic characteristic for up-spin channel. Therefore CuMnO_2 would behave like half-metallic ferromagnetic material with 100% spin polarization. It is important to mention that half-metallic ferromagnets (HMFM) is essential for spintronic devices^{33,34}. In particular CuMnO_2 can be used as a spin injector for spin valves in opto-spintronic devices. In the down-spin channel, valence band maxima (VBM) lies at Y_2 point and conduction band minima (CBM) lie at Γ point which indicates the indirect band gap semiconducting behavior

of CuMnO_2 for down-spin channel. The indirect band gaps in the down-spin channel (along $Y_2 - \Gamma$ symmetry), obtained under GGA and GGA+U approximations are found to be 1.08 eV and 2.22 eV, respectively.

The half-metallic behavior of CuMnO_2 arises due to the hybridization process that occurs between O-2p states and Mn-3d states. The hybridization mainly occurs through the *double exchange* mechanism³⁵. As already mentioned, in each MnO_6 octahedra Mn^{+3} ions are in the $t_{2g}^3 e_g^1$ configurations. The 3 electrons in the t_{2g} manifold effectively forms a core spin with $S = 3/2$. According to Anderson-Hasegawa model³⁶ for double exchange electrons in singly occupied e_g manifold is strongly coupled with t_{2g} core spin through Hund's coupling J_H . In the limit $J_H \rightarrow \infty$ the spin of the e_g electron gets effectively locked with the core spin and the effective hopping amplitude between two Mn atoms (via O atoms) gets reduced by a factor $\cos(\theta/2)$, where θ is the angle between two core spins. Under this scenario conduction through only one spin channel is allowed and the bands corresponding to other spin channel gets completely integrated out. For finite J_H the energy bands corresponding to the unfavourable spin channel gets gapped out at the Fermi level and the energy gap is proportional to J_H .

The observed features of the electronic band structure can be easily explained in terms of the scenario presented above. In the ferromagnetic phase the spins were in the up configuration there by making the up spin channel favourable and the down spin channel unfavourable. This will give rise to 100% spin polarized transport through up spin channel while the down channel will be gapped out. The energy gap will be directly proportional to effective Hund's coupling strength. In the presence of U [under GGA+U approximation] the gap further enhances due to Coulomb energy cost for double occupancy.

In Fig. 7 we have plotted total as well as partial density of states (pDOS) for various atoms under GGA [panel (a)] and GGA+U [panel (b)] approximations. We also have shown orbital resolved pDOS for each atom. A detailed plot in a reduced energy window in Fig. 8 shows that the density of states for the up spin channel under GGA approximation [panel (a)] is small but finite while the same under GGA+U approximation [panel (b)] vanishes at the Fermi level. The density of states in both the cases shows asymmetric power law behaviour at the Fermi level which is a characteristics of the half-metallic state. The density of states for the down spin channel shows a clear gap at the Fermi level under both GGA and GGA+U approximation. The power law behaviour of up spin density. The up spin density of states arises due hybridization between Mn-3d and O-2p orbitals. In particular Mn- $d_{x^2-y^2}$ and O- $2p_x$ hybridized orbital makes dominant contribution to density of states at the Fermi level. This p-d hybridization plays vital role to stabilize the half-metallic ferromagnetism in CuMnO_2 . In addition to the above, one can see that Cu-3d states have negligible contribution in conduction as well as valence band to the total DOS for both the spin channels near

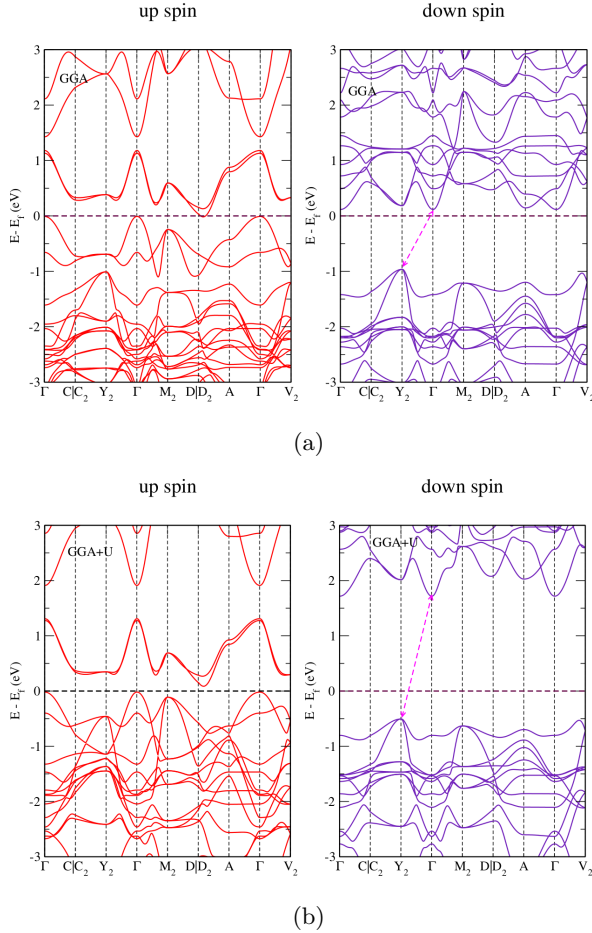


FIG. 6: Electronic band structure in the ferromagnetic state of CuMnO_2 , calculated under GGA [panel (a)] and GGA+U [panel (b)] approximations. The top of the valence band is set to 0 eV.

Fermi level. This p-d hybridization plays vital role to stabilize the half-metallic ferromagnetism in CuMnO_2 .

V. MAGNETIC PROPERTIES

We also have calculated magnetic moment per unit cell as well as magnetic moment of individual atoms in both the phases. In Tab. III we have shown the total magnetic moment per unit cell (M_{tot}) and the magnetic moments contributed by the individual atom for both the ferromagnetic and antiferromagnetic state of CuMnO_2 . As can be clearly seen the main contribution of total magnetic moment is due to the Mn atoms whereas the induced magnetic moments on Cu and O atoms are negligibly small. As already mentioned due to crystal field effects each Mn^{+3} ion is in $t_{2g}^3 e_g^1$ configuration. The electrons in 3 fold degenerate t_{2g} orbital forms a core spin with $S = 3/2$ and magnetic moment $3\mu_B$. The electron in e_g orbital hybridizes with neighbouring O atoms. Also

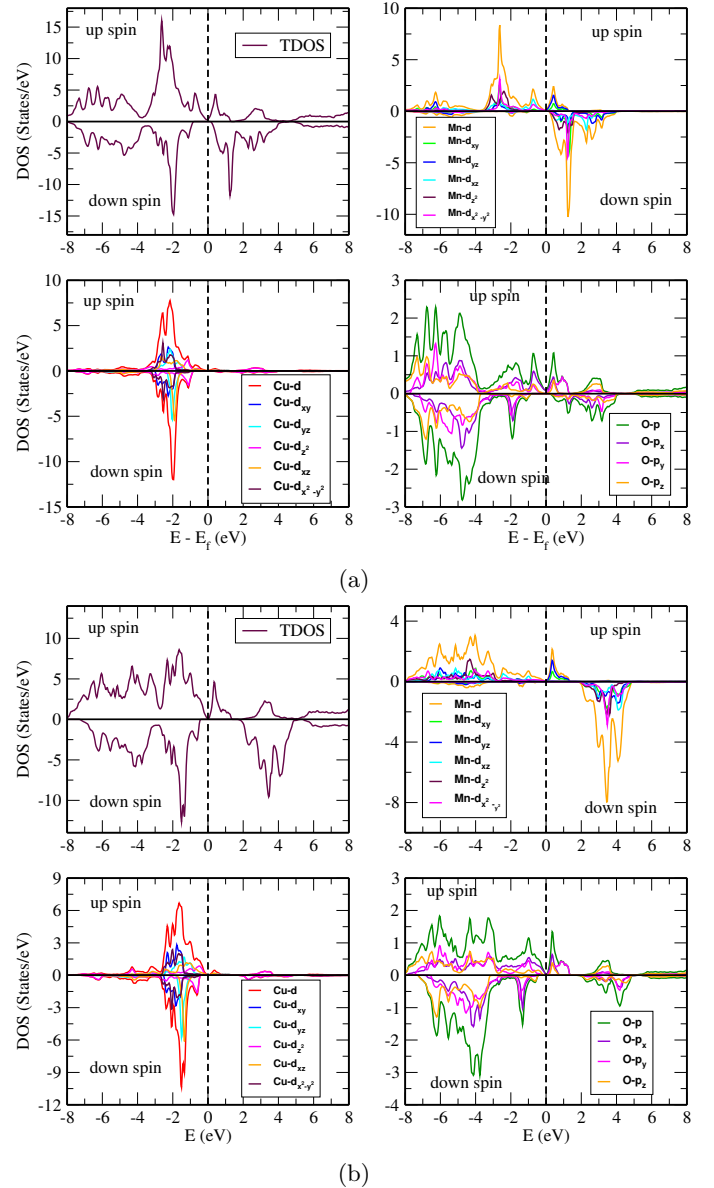


FIG. 7: Total and partial density of states of CuMnO_2 in the ferromagnetic state, calculated under GGA [panel (a)] and GGA+U [panel (b)] approximations. Detailed orbital contribution of each atom in a given unit cell are also shown.

two layers of MnO_6 octahedra are connected via O-Cu-O bond along the c -axis. Interestingly, in the ferromagnetic state total induced moment on 6 oxygen atom and a Cu atom is exactly equal to the missing $0.301\mu_B$ moment for each e_g electrons. The calculated magnetic moments are very close to the reported values.

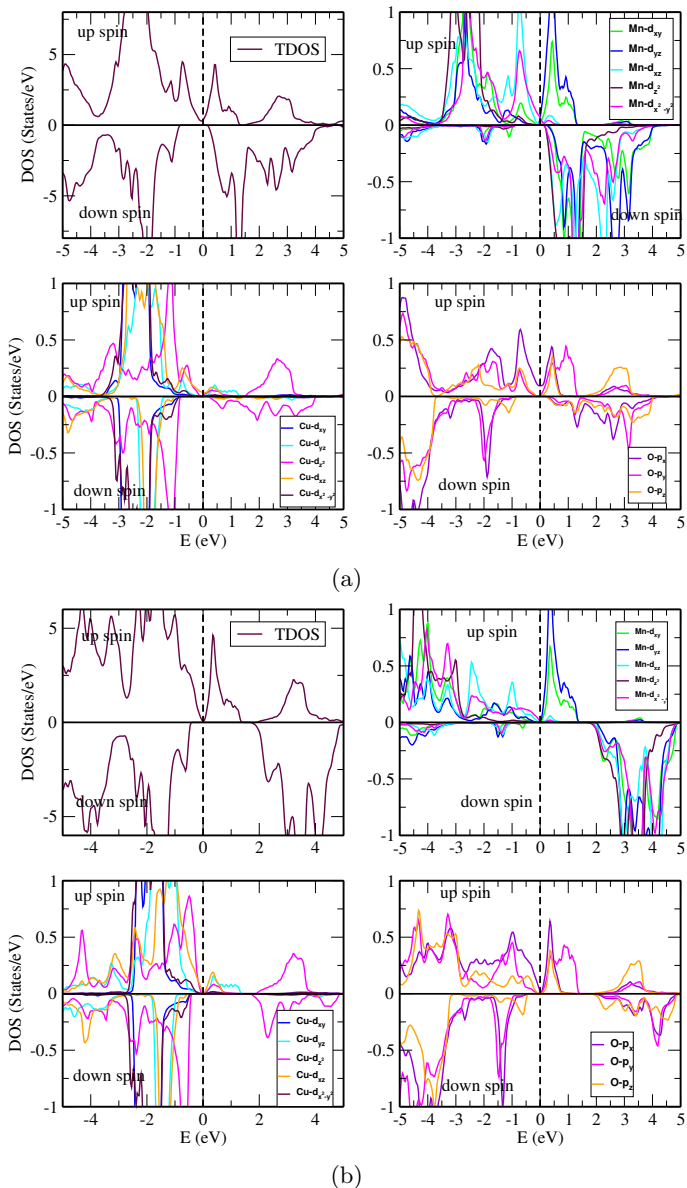


FIG. 8: Same plot as in Fig 7 but in a reduced energy window. Reduced energy window has been chosen to enhance the clarity of orbital resolved partial DOS near the Fermi level.

VI. CONCLUSIONS

To summarize, we have calculated the electronic band structures and density of states of CuMnO_2 in both the ferromagnetic and antiferromagnetic states under GGA and GGA+U approximation. The lattice parameters obtained from relaxed structures show good agreement with other theoretical and experimental results. The electronic band structure in the antiferromagnetic state shows semiconducting behaviour with indirect band gap - consistent with experimental observations. However the calculated band gap (~ 0.5 eV) overestimates the ex-

TABLE III: Calculated magnetic moment of individual atom and total magnetic moment of CuMnO_2 .

Systems	Cu (μ_B)	Mn (μ_B)	O (μ_B)	M_{Tot} (μ_B)
CuMnO_2 (FM)	0.019	3.699	0.047	7.624
CuMnO_2 (AFM)	0.016	3.574	0.024	0.0

perimentally observed value. This is due to the inadequacy of the exchange-correlation function used under GGA approximation. The orbital resolved partial density of states shows that the valence band arises predominantly due to hybridization between $\text{Mn-}3d_{x^2-y^2}$ and $\text{O-}2p_x$ orbitals, whereas the conduction bands arise due to hybridized $\text{Mn-}3d$ and $\text{O-}2p$ states. The broad peaks in the conduction band arise due to transition between crystal field split $\text{Mn-}3d$ orbitals. $\text{Cu-}3d$ orbitals have minor contribution to valence bands and practically no contribution to conduction bands.

The electronic band structure in the ferromagnetic state shows band gap in the down spin channel whereas the bands in the up spin channel touches the Fermi level. This behavior is consistent with half-metallic state with 100% spin polarization in the ferromagnetic phase. The half metallicity arises due to *double exchange* mechanism in which the e_g electron spin is strongly coupled to the t_{2g} core spin through Hund's coupling, J_H . This facilitates conduction of up spin electrons while the conduction down spin electrons costs an energy J_H . As a result the energy bands for the up spin channel is gap less while that for the down spin bands are gapped. Due to this unique behavior, CuMnO_2 in the ferromagnetic state has a potential application as a spin injector for spin valve in spintronic devices. The density of states near the Fermi level shows asymmetric power law behaviour. From the orbital resolved partial density of states we infer that hybridized $\text{Mn-}d_{x^2-y^2}$ and $\text{O-}2p_x$ orbital gives rise to bands near the Fermi level.

We also have calculated the total magnetic moment for a given unit cell as well as magnetic moment of individual atoms in the both the antiferromagnetic and ferromagnetic state. In the ferromagnetic state the magnetic moment of Mn atoms $3.699\mu_B$ arises due to localised t_{2g} electrons ($3\mu_B$) and itinerant e_g electrons while the induced magnetic moment on O and Cu atoms arises due to hybridization on e_g electrons with $\text{O-}2p$ orbitals along the Mn-O-Mn bond and hybridization between $\text{O-}2p$ and $\text{Cu-}3d$ orbitals along the O-Cu-O bonds connecting two layers of MnO_6 octahedra.

VII. ACKNOWLEDGEMENTS

We would like to thank Kazi Nazrul University for partial research support. One of us (A.S) would like to thank UGC, Government of India for providing financial support. One of us (N.P) would like to thank IIT, Kharagpur for providing hospitality where part of the manuscript

was written.

-
- ¹ Sajad Ali, Hayat Ullah, Abeer A AlObaid, and Tahani I Al-Muhimeed. *The European Physical Journal Plus*, **136**:1, (2021).
- ² A Benmakhlouf, Y Bourourou, A Bouhemadou, A Bentabet, F Khemloul, S Maabed, M Bouchenafa, and I Galanakis. *Journal of Magnetism and Magnetic Materials*, **465**:430, (2018).
- ³ Bisma Tariq, G Murtaza, Hassan Ali, Samia Razzaq, RM Arif Khalil, Muhammad Iqbal Hussain, Khawar Ismail, Ghazanfar Nazir, and Nouf H Alotaibi. *Solid State Communications*, **370**:115229, (2023).
- ⁴ Khawar Ismail, Hind Albalawi, G Murtaza, Tahani I Al-Muhimeed, Abeer A AlObaid, and Q Mahmood. *Physica Scripta*, **96**:095802, (2021).
- ⁵ Amol P Amrute, Zbigniew Lodziana, Cecilia Mondelli, Frank Krumeich, and Javier Perez-Ramirez. *Chemistry of Materials*, **25**:4423, (2013).
- ⁶ Juliano Schorne-Pinto, Laurent Cassayre, Lionel Presmanes, and Antoine Barnabé. *Inorganic Chemistry*, **58**:6431, (2019).
- ⁷ Ian Sullivan, Brandon Zoellner, and Paul A Maggard. *Chemistry of Materials*, **28**:5999, (2016).
- ⁸ Dehua Xiong, Zijuan Du, Hong Li, Junyuan Xu, Junjie Li, Xiujian Zhao, and Lifeng Liu. *ACS Sustainable Chemistry & Engineering*, **7**:1493, (2018).
- ⁹ Yasuhiko Takahashi, Yoshito Gotoh, and Junji Akimoto. *Journal of Solid State Chemistry*, **172**:22, (2003).
- ¹⁰ Shinichiro Seki, Yoshinori Onose, and Yoshinori Tokura. *Physical review letters*, **101**:067204, (2008).
- ¹¹ Jason T Haraldsen, Feng Ye, Randy S Fishman, Jaime A Fernandez-Baca, Yasuhiro Yamaguchi, Kenta Kimura, and Tsuyoshi Kimura. *Physical Review B*, **82**:020404, (2010).
- ¹² Haowen Wang, Chengliang Lu, Jun Chen, Yong Liu, SL Yuan, Sang-Wook Cheong, Shuai Dong, and Jun-Ming Liu. *Nature communications*, **10**:2280, (2019).
- ¹³ A Zorko, J Kokalj, M Komelj, O Adamopoulos, H Luetkens, D Arçon, and A Lappas. *Scientific reports*, **5**, (2015).
- ¹⁴ M Poienar, R Banica, P Sfirloaga, C Ianasi, CV Mihali, and P Vlazan. *Ceramics International*, **44**:6157, (2018).
- ¹⁵ Sumio Kato, Ryu Fujimaki, Masataka Ogasawara, Takashi Wakabayashi, Yuunosuke Nakahara, and Shinichi Nakata. *Applied Catalysis B: Environmental*, **89**:183, (2009).
- ¹⁶ Françoise Damay, Maria Poienar, Christine Martin, Antoine Maignan, J Rodriguez-Carvajal, Gilles André, and Jean-Pierre Doumerc. *Physical Review B*, **80**:094410, (2009).
- ¹⁷ AV Ushakov, SV Streltsov, and DI Khomskii. *Physical Review B*, **89**:024406, (2014).
- ¹⁸ H Hiraga, T Fukumura, A Ohtomo, T Makino, A Ohkubo, H Kimura, and M Kawasaki. *Applied Physics Letters*, **95**, (2009).
- ¹⁹ I. Fina, X. Marti, D. Yi, J. Liu, J. H. Chu, C. Rayan-Serrao, S. Suresha, A. B. Shick, J. Železný, T. Jungwirth, J. Fontcuberta, and R. Ramesh. *Nature Communications*, **5**:4671, (2014).
- ²⁰ Sandip Aryal, Durga Paudyal, and Ranjit Pati. *Nano Letters*, **21**:1856, (2021).
- ²¹ *Computational and Theoretical Chemistry*, **1197**:113155, (2021).
- ²² Dongke Chen, Zhengyu Jiang, Ying Tang, Junlei Zhou, Yuzhou Gu, Jing-Jing He, and Jiaren Yuan. *Frontiers in Chemistry*, **10**, (2022).
- ²³ Maylis Orío, Dimitrios A Pantazis, and Frank Neese. *Photosynthesis research*, **102**:443, (2009).
- ²⁴ Khawar Ismail, Ayesha Parveen, Ayesha Zia, Samia Razzaq, Ghulam Murtaz, Syed Muzahir Abbas, and Javad Feroz. *Applied Physics A*, **129**:676, (2023).
- ²⁵ Jürgen Hafner. *Journal of computational chemistry*, **29**:2044, (2008).
- ²⁶ Matthias Ernzerhof and Gustavo E Scuseria. *The Journal of chemical physics*, **110**:5029, (1999).
- ²⁷ John P Perdew, Kieron Burke, and Matthias Ernzerhof. *Physical review letters*, **77**:3865, (1996).
- ²⁸ Peter E Blöchl. *Phys. Rev. B*, **50**:17953, (1994).
- ²⁹ Hendrik J Monkhorst and James D Pack. *Physical review B*, **13**:5188, (1976).
- ³⁰ Koichi Momma and Fujio Izumi. *Journal of applied crystallography*, **44**:1272, (2011).
- ³¹ C. Vecchini, M. Poienar, F. Damay, O. Adamopoulos, A. Daoud-Aladine, A. Lappas, J. M. Perez-Mato, L. C. Chapon, and C. Martin. *Phys. Rev. B*, **82**:094404, (2010).
- ³² M. Poienar, C. Vecchini, G. André, A. Daoud-Aladine, I. Margiolaki, A. Maignan, A. Lappas, L. Chapon, M. Hervieu, F. Damay, and C. Martin. *Chemistry of Materials*, **23**:85, (2011).
- ³³ S. A. Wolf, D. D. Awschalom, R. A. Buhrman, J. M. Daughton, S. von Molnár, M. L. Roukes, A. Y. Chtchelkanova, and D. M. Treger. *Science*, **294**:1488, (2001).
- ³⁴ Warren E. Pickett and Jagadeesh S. Moodera. *Physics Today*, **54**:39, (2001).
- ³⁵ Hardev S Saini, Poonam Poonam, AK Pundir, Mukhtiyar Singh, Jyoti Thakur, and Manish K Kashyap. In *AIP Conference Proceedings*, volume **2115**. AIP Publishing, 2019.
- ³⁶ P. W. Anderson and H. Hasegawa. *Phys. Rev.*, **100**:675, (1955).